Chemical Synthesis

Research Article

Alkalinity-controlled zeolite nucleation and growth: ultrafast synthesis of total-morphology zeolite L mesocrystals and adsorption evaluation

Zhaoqi Ye[1,#], Lingtao Kong[1,#], Yang Zhao[1], Chunna Zhang[1], Xue Yang[1], Kexin Yan[1], Yahong Zhang[1], Hongbin Zhang[2,*] (ID)**, Yi Tang[1,*]** (ID)

[1]Department of Chemistry, Laboratory of Advanced Materials, Collaborative Innovation Center of Chemistry for Energy Materials and Shanghai Key Laboratory of Molecular Catalysis and Innovative Materials, Fudan University, Shanghai 200433, China.
[2]Institute for Preservation of Chinese Ancient Books, Fudan University Library, Fudan University, Shanghai 200433, China.
[#]Both authors contributed equally to this work.

*Correspondence to: Prof. Yi Tang, Department of Chemistry, Laboratory of Advanced Materials, Collaborative Innovation Center of Chemistry for Energy Materials and Shanghai Key Laboratory of Molecular Catalysis and Innovative Materials, Fudan University, Shanghai 200433, China. E-mail: yitang@fudan.edu.cn; Dr. Hongbin Zhang, Institute for Preservation of Chinese Ancient Books, Fudan University Library, Fudan University, Shanghai 200433, China. E-mail: zhanghongbin@fudan.edu.cn

Abstract

Owing to the intrinsic complexity of crystallization and the heterogeneity of precursors, the specific stages and corresponding behaviors of an actual crystallization system remain ambiguous, which makes the univariate-controlled crystallization-kinetics-regulated synthesis and design of zeolite morphology and porosity an unrealized blueprint. In this study, a facile and univariate modulation (i.e., OH^-/SiO_2) strategy was developed to regulate zeolite crystallization kinetics, and zeolite L mesocrystals were synthesized rapidly (within 1-2 h) with almost all **LTL** morphologies (from cylindrical or disc-like shapes to nanoclusters or nanocrystals) in the simplest SiO_2-Al_2O_3-K_2O-H_2O system. Using time-resolved analysis of the change in the solid-liquid Si/Al nutrient and crystallinity evolution, the intertwined and complex crystallization processes of zeolite L were clearly distinguished into four distinct stages: induction, nucleation, growth, and ripening. Under alkalinity-controlled conditions, the reactivity, Si/Al distribution, and state of aluminosilicates were critical to the formation of short-range order in the amorphous matrix, which greatly influenced the nucleation frequency and assembly state. Subsequently, these nucleation differences evoked correspondingly different kinetic growth behaviors. A putative alkalinity-controlled nonclassical crystallization mechanism was uncovered, and its validity was evaluated by analyzing morphology

evolution, NH_4F etching, and the effects of modifiers. Furthermore, adsorption tests demonstrated the high adsorption capacity of a series of zeolite L for guest molecules with various sizes and properties (e.g., gaseous aromatic hydrocarbon, aqueous dye, and protein).

INTRODUCTION

Exploring the crystallization mechanism is one of the most fundamental and vital parts of research on crystalline materials because it leads to endless possibilities for the engineering and functionalization of material structures[1-7]. In the crystallization system of inorganic materials, such as zeolites, it is widely accepted that crystal growth not only depends on the addition of simple ions or small molecules (classical crystallization mechanism[8,9]) but also involves the assembly of a series of more complex and evolvable "particles"[9,10] - including crystalline[11], semi-crystalline[12] or amorphous oligomers, clusters, and nanoparticles[13] (nonclassical crystallization mechanism). These particles attach to the surface of nuclei with a certain spatial orientation[14-16], forming orderly assembled superstructure crystals with nanoparticles as the basic unit, i.e., mesocrystals[17-19]. If we can comprehensively understand and effectively control the nonclassical assembly behavior of crystal materials, then it will be possible to pre-design mesocrystal products with configurable morphologies targeting specific applications.

With the aim of reducing the diffusion limitation of zeolites and regulating the properties of zeolites for macromolecular adsorption and liquid-phase reactions, the last two decades have witnessed researchers devising different ways to introduce mesopores into zeolitic microporous systems[20], such as designing novel organic structure-directing agents[21-23], using mesopore-directing templates[24-26], and implementing post-treatments[27-29]. Compared with these intricate methods, it is a more promising approach to construct zeolite mesocrystals with special morphologies and pore structures solely and simply based on nonclassical crystallization mechanisms, which is a low-cost and green alternative requiring neither special templates nor re-dissolving of the crystalline part. There has been excellent progress in developing novel zeolite materials under this blueprint. For instance, Zhang *et al.* revealed the evolution of the structure and size of precursor particles in the nonclassical crystallization process of ZSM-5[30-33]. Meanwhile, Kumar *et al.* modulated the size and morphology of SSZ-13[34], zeolite L[35], and SAPO-34[36] by using recyclable organic modifiers to regulate the aggregation growth of precursor particles. In our previous works, a series of ZSM-5 mesocrystals were synthesized under the seed-induced synthesis route by using inorganic cations to modulate the assembly behavior[37,38], and ZSM-12 mesocrystals with a clustered, fractal, or finned structure were obtained by tuning the concentration-dependent crystallization kinetics[39-41]. However, owing to the intrinsic complexity of the zeolite synthesis system, different stages of the crystallization process - namely induction, nucleation, growth, and ripening - are often intertwined and exhibit significant interplay[30]. Ambiguous understanding of the crystallization behavior of zeolites hinders the realization of thermodynamic and kinetic control of the crystallization process.

According to current studies on the crystallization mechanism, zeolite L (**LTL** type) is a potential model of zeolite growth owing to its widely tunable morphology and special crystallization habit. Specifically, as a typical zeolite with a Si/Al ratio (denoted as SAR) of 2.0-4.0, zeolite L generally needs to be produced in a precursor system with a higher SAR (≥ 10), and the elemental composition of the product is relatively fixed and unaffected by the synthesis conditions[42-44]. Therefore, the crystallization stage can be monitored by simply tracking SAR changes. Moreover, as a 1D channeled zeolite (12-membered ring, ~0.7 nm in width,

oriented axially along the *c*-axis) with a hexagonal crystal structure, zeolite L exhibits anisotropic growth along the *c*-axis, which facilitates determination of the crystal axis direction of both the products and intermediates under electron microscopes[45]. In addition, past studies have reported zeolite L with multiple morphologies, from nanoclusters to micron-sized cylinders[42-44,46], which provides sufficient space to explore and clarify intrinsic factors and mechanisms for crystal regulation. Although nonclassical particle-assemble crystallization (CPA) of zeolite L with particular morphologies, especially micron-sized cylinders, has been observed and preliminarily exploited[35,47], more specific nucleation and growth behaviors at different crystallization stages under differential synthesis conditions are still missing, and thus the intrinsic factors leading to different morphologies remain uncovered.

In this study, alkalinity-controlled crystallization kinetics regulation was developed to achieve ultrafast and total-morphology synthesis of zeolite L mesocrystals with widely tunable sizes and morphologies, from cylindrical or disc-like shapes to nanoclusters or nanocrystals. This novel strategy entails simply and strategically changing KOH/SiO_2. Serendipitously, by investigating the relative crystallinity of intermediates and the dynamic concentration change of nutrient species in the solid and liquid phases, we found that the crystallization process of zeolite L can be divided clearly and explicitly into four stages: induction, nucleation, growth, and ripening. By systematically detecting the formation of microstructures and thoroughly investigating crystallization and dissolution processes, we established that the nucleation-growth process is thermodynamically and kinetically regulated through the alkalinity of the synthesis system. Moreover, a related nonclassical crystallization mechanism was revealed, and its validity was evaluated by investigating morphology evolution, NH_4F etching, and the effects of modifiers and K^+. Furthermore, the high adsorption capacities of zeolite L mesocrystals with different morphologies for gaseous aromatic hydrocarbons, liquid dye, and protein molecules were confirmed, which further demonstrated the effectiveness and potential utility of this method in tailoring the zeolite size and morphology.

EXPERIMENTAL

Materials

Fumed silica (Aerosil400, Shanghai Chlorine Alkali Industry), aluminum foil (SP grade, Aladdin), potassium hydroxide (KOH, semiconductor grade, Aladdin), sodium hydroxide (NaOH, AR grade, Aladdin), and deionized water were employed for the preparation of zeolite L. Poly dimethyl diallyl ammonium chloride (PDDAC, M.W. 100-200 k, 20 wt% in water, Aladdin), *n*-butylamine (*n*-$BuNH_2$, GC grade, Aladdin), and ammonium fluoride (NH_4F, AR grade, Aladdin) were used to verify the crystallization mechanism. Additionally, *o*-xylene (GC grade, Aladdin), 1,3,5-triethyl benzene (GC grade, Aladdin), methylene blue (AR grade, Macklin), myoglobin (from horse skeletal muscle, salt-free, lyophilized powder, Sigma), ammonium acetate (NH_4OAc, 40 wt% aqueous solution, Aladdin), potassium phosphate monobasic (KH_2PO_4, AR grade, Aladdin), and phosphoric acid (H_3PO_4, AR grade, Aladdin) were employed in multiple adsorption tests.

Synthesis of samples

Zeolite samples were synthesized in a $xKOH/0.0667Al/1.00SiO_2/20.0H_2O$ system, where x (OH^-/SiO_2 ratio, BSR) = 0.65-1.35, and the resulting samples are denoted as **LTL-*x***. In detail, a certain amount of KOH was dissolved in water, and the resulting solution was divided equally into two parts. Then, a clear aluminate solution was prepared by adding the aluminum foil to one part of the KOH solution. Meanwhile, the fumed silica was added to the other part of the KOH solution with stirring and heating at 80 °C for 1 h to dissolve SiO_2 completely, and a clear silicate solution was obtained. After cooling to room temperature, the above-mentioned clear aluminate solution was slowly added to the clear silicate solution with vigorous stirring. The obtained clear solution was aged at room temperature with stirring for 12 h and then heated to 190 °C in a Teflon-lined autoclave for a certain time (see Supplementary Table 1). After hydrothermal treatment,

the zeolite L products were separated by centrifugation (15,000 rpm for 40 min with a relative centrifugal force of $19118 \times g$) and washed with deionized water several times. To study the difference in the crystallization behavior of zeolite L in different basicity ranges, two typical samples were selected and further denoted as **LTL-LB** (x = 0.75) and **LTL-HB** (x = 1.15). The crystallization intermediates were extracted at the pre-determined time and denoted as **LTL-LB/HB-t**, where t (min) refers to the heating time. To minimize structural changes in the collected samples, especially the intermediates, all washed samples were freeze-dried in a vacuum at -50 °C.

Characterization

Powder X-ray diffraction (XRD) experiments of the as-synthesized samples were conducted on a Bruker D2 diffractometer (Cu-K$_\alpha$, 10 kV, 30 mA) from 5° to 50°. The morphologies and surface features of the samples were monitored by using field-emission scanning electron microscopy (FE-SEM, Hitachi S-4800), and structural features were visualized by using field-emission transmission electron microscopy (FE-TEM, Tecnai G2 F20 S-Twin). Selected area electron diffraction (SAED) and spot elemental analysis by energy dispersive spectroscopy (EDS) was conducted on a Tecnai G2 F20 S-Twin instrument to investigate the fine structure of the products. Fourier transform infrared spectra (FT-IR) were recorded on a PerkinElmer Frontier IR instrument with a resolution of 4 cm^{-1} in the range of 1000-400 cm^{-1}. The physical parameters and porous structure of the products and intermediates were determined by using a Quantachrome iQ-2 instrument to conduct N_2-sorption experiments at 77 K and Ar-sorption experiments at 87 K after outgassing at 573 K for 8 h. Changes in the concentration of species in the supernatant liquid separated from the mixture by centrifugation and the element ratio in the solid phase were analyzed by using inductively coupled plasma-atomic emission spectrometry (ICP-AES, iCAP 7400). Raman spectra were recorded with a Horiba Jobin Yvon XploRA confocal microscope equipped with a 532 nm laser. ^{27}Al MAS NMR spectra were acquired on a Bruker DSX 300 spectrometer.

Zeolite adsorption tests

Adsorption of *o*-xylene (0.65 nm) and 1,3,5-triethyl benzene (0.82 nm) in zeolite L was evaluated by using a gravimetric gas sorption analyzer (IGA, Hiden Analytical). The sample was degassed under a vacuum of less than 10^{-3} Pa at 673 K for 2 h before the adsorption measurement.

The adsorption capacity of the zeolites was determined by measuring the ultraviolet-visible (UV-vis, PE-Lamnda 35, PerkinElmer) absorption spectra of methylene blue (1.43 nm × 0.61 nm × 0.40 nm) over zeolite L samples and by calculating the concentrations of methylene blue from the absorption peak at λ = 661 nm. In detail, 20 mg of LTL mesocrystals were added to a conical flask, and then 10 mL of methylene blue (1.00-35.0 mg/L, in 0.02 mol/L NH$_4$OAc aqueous solution, pH = 7.0) was added quickly. After that, the suspensions were stirred vigorously at room temperature for a pre-determined time (for the isotherm measurement, the adsorption time was 12 h). The protein adsorption capability of zeolite L was determined by incubating myoglobin (0.1 mg/mL, 4.5 nm × 3.5 nm × 2.5 nm) and zeolite L (0.1 mg/mL) mixtures in phosphate-buffered saline (PBS, 20 mmol/L, pH = 5.0) for 1.0 h at room temperature. After centrifugation, the UV-vis absorbance value (λ = 409 nm) of the supernatant was measured to calculate the amounts of protein adsorbed on zeolite L.

RESULTS AND DISCUSSION

Fast synthesis of zeolite L with total morphologies

By optimizing the mixing and aging of K$^+$-contained aluminosilicate precursors, univariate modulation (OH$^-$/SiO$_2$ ratio, denoted as BSR) of the crystallization process was achieved for the fabrication of a series of L zeolites [Figure 1] in the simplest SiO$_2$-Al$_2$O$_3$-K$_2$O-H$_2$O system. Herein, the resulting products are denoted as LTL-x, where x is the BSR value. The obtained zeolite L mesocrystals display widely tunable sizes and
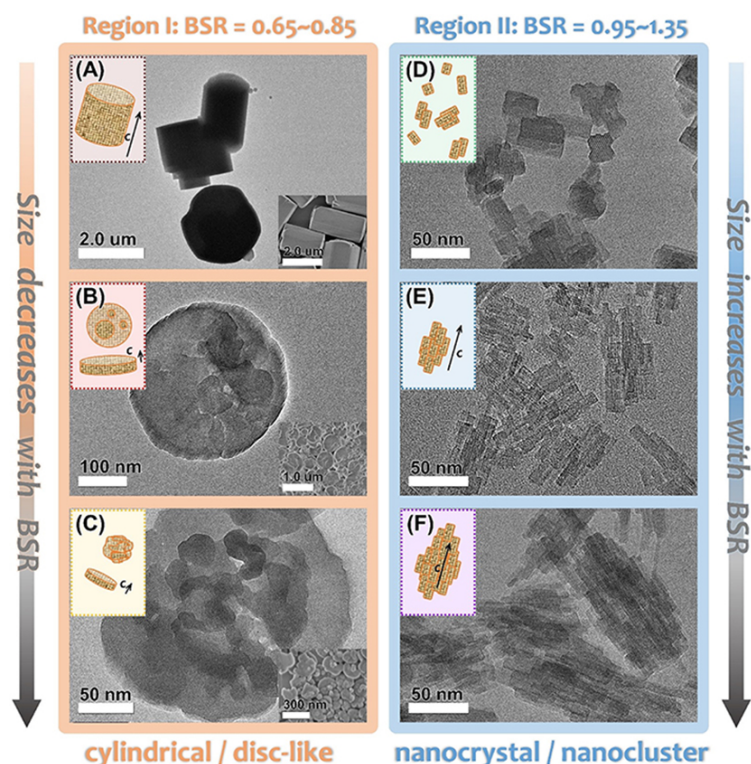
Figure 1. TEM images of zeolite L products synthesized under different alkalinity conditions. BSR equals (A) 0.65, (B) 0.75, (C) 0.85, (D) 0.95, (E) 1.15, and (F) 1.35. Inset of (A)-(C): corresponding SEM images.

morphologies, from cylindrical or disc-like shapes to nanoclusters or nanocrystals, covering all morphologies reported so far. Moreover, most morphologies can be rapidly prepared with a heating time as short as 1 to 2 h at 190 °C. Compared with reported synthesis conditions [Supplementary Table 1], the overall crystallization rate of the optimized system is faster, and K^+ is used as the only inorganic structure-directing agent without additional organic modifiers.

Interestingly, with the adjustment of alkalinity (BSR from 0.65 to 1.35), the architectural feature of zeolite L seems to obey a piecewise size-change rule in two BSR regions with different dominant morphologies. When BSR ≤ 0.85 [Figure 1A-C], the morphology of zeolite L products is cylindrical or disc-shaped. Additionally, the particle size undergoes a dramatic decline from ~(1.5-2.0) μm × (1.5-2.0) μm (diameter along a/b-axis × length along c-axis, denoted as $d × l$) to ~300 nm × 100 nm and ~200 nm × (50-60) nm as the alkalinity increases from 0.65 to 0.75 and 0.85. In detail, for LTL-0.65 and LTL-0.75, the product crystals have smooth and regular edges [Figure 1A and B]. High-resolution TEM (HR-TEM) images further reveal aligned and coherent lattice fringes, and SAED results also show pure **LTL**-phase diffraction patterns [Supplementary Figure 1A and B], indicating that LTL-0.65/0.75 have single-crystal-like structures and dense, coherent textures. When BSR reaches 0.85, the corresponding zeolite product remains disc-like but becomes partially fragmented [Figure 1C]. In the high alkalinity region (BSR ≥ 0.95), however, zeolite L nanoparticles and nanoclusters are obtained, and a converse change in the size is observed. The products reach the minimum size of ~15 nm × (30-35) nm when BSR = 0.95 [Figure 1D]. Further increasing the alkalinity reduces the size of the crystal domains to some extent but also increases the tendency of these nanoparticles to form clusters. As the BSR increases to 1.15 and 1.35, the overall size of the nanoclusters improves to ~(30-40) nm × (60-80) nm and ~(60-70) nm × (100-120) nm, respectively [Figure 1E and F]. Notably, within a single cluster assembly, the lattice orientations of adjacent domains are aligned

[Supplementary Figure 1C and D], indicating oriented growth instead of random aggregation for these nano-units.

The XRD patterns of all samples contain only diffraction peaks corresponding to the **LTL** phase [Figure 2A], and broadening of the diffraction peaks is mainly due to the nanosized crystal domains, especially under high BSR. Moreover, N_2-sorption experiments show that the porosity of the products is effectively regulated by simply adjusting the system basicity [Figure 2B]. Except for LTL-0.65, the other five samples show typical isotherms with type I and IV features, which indicates the coexistence of micro- and mesopores[48]. The isotherm of LTL-0.65 exhibits only type I characteristics, which indicates a micron-sized and dense zeolite structure[48]. As BSR gradually increases, the uptake at high p/p_0 increases, suggesting gradual enrichment of mesoporosity. Detailed texture data [Supplementary Table 2] further confirm the above results. In the BSR range of 0.65 to 1.35, the mesopore volume (V_{meso}) of the obtained products increases from 0.012 to 0.755 cm³/g, and the external surface area (S_{ext}) grows from 9 to 246 m²/g. It is worth noting that, although the overall particle sizes of zeolites slightly increase in the high BSR region, V_{meso} and S_{ext} do not decrease but enlarge, indicating that adjacent domains are loosely combined rather than fully fused. In addition, the rise in alkalinity somehow affects the microporosity of products because of the drop in the micropore volume (V_{micro}) from ~0.14 to ~0.09 cm³/g. Increasing the alkalinity significantly reduces the size of LTL zeolites and simultaneously produces many defects inside the LTL crystal, such as point defects and dislocations, leading to the existence of mesopores and macropores among adjacent domains, as shown in the inset of Figure 2B (pore size distribution of LTL-HB). These gradually increasing defects and decreasing LTL zeolite size largely lead to a reduction in the micropore volume.

LTL-LB (BSR = 0.75) and LTL-HB (BSR = 1.15) were selected as representative samples for further pore structure analysis. The mesopore size distribution (Figure 2B, inset) shows that the mesopore size in LTL-HB is distributed over 5-30 nm, attributed to the assembly structure of ultra-small nanocrystals [Figure 1E]. LTL-LB has fewer meso- and macropores, which is related to its larger particle size, denser crystal structure, and smoother surface features. Moreover, the micropore size distribution by Ar-sorption [Supplementary Figure 2] shows that both products have characteristic **LTL** micropores of 0.7-0.8 nm, which are slightly larger in LTL-HB than in LTL-LB, suggesting that more crystal defects and incomplete pore walls are created at higher alkalinity conditions. Additionally, the micropore distribution of LTL-HB exhibits a more pronounced maximum in the range of 1.0-1.5 nm [Supplementary Figure 2], which may originate from the voids between adjacent nanodomains.

The **LTL** structure of samples is further confirmed by FT-IR experiments [Supplementary Figure 3]. The absorption bands at 609 and 648 cm⁻¹ are attributed to the double six-membered ring (**d6r**) vibration due to the external linkage, and the absorption bands at 725 and 772 cm⁻¹ can be assigned to the symmetric T-O (T = Si or Al) stretching vibrations from the external tetrahedral linkage[49,50]. Moreover, the intensity and frequency of these absorption bands are sensitive to the chemical composition of zeolite[51]. As BSR increases, the above-mentioned absorption bands gradually shift to lower wavenumbers accompanied with weaker intensities, indicating a decrease in product SAR[51]. This tendency is also revealed through the elemental analysis. As BSR increases sharply from 0.65 to 1.35, the SAR of the samples decreases slightly from 2.60 to 2.29 [Supplementary Table 2], showing that the system basicity does have a certain effect on the SAR of zeolite L (but not significant), which is consistent with previous reports[42-44].

Time-resolved investigation of zeolite L crystallization
Identification of different stages in the crystallization process
To elucidate the detailed discrepancies in the crystallization mechanism in different BSR regions, we tracked
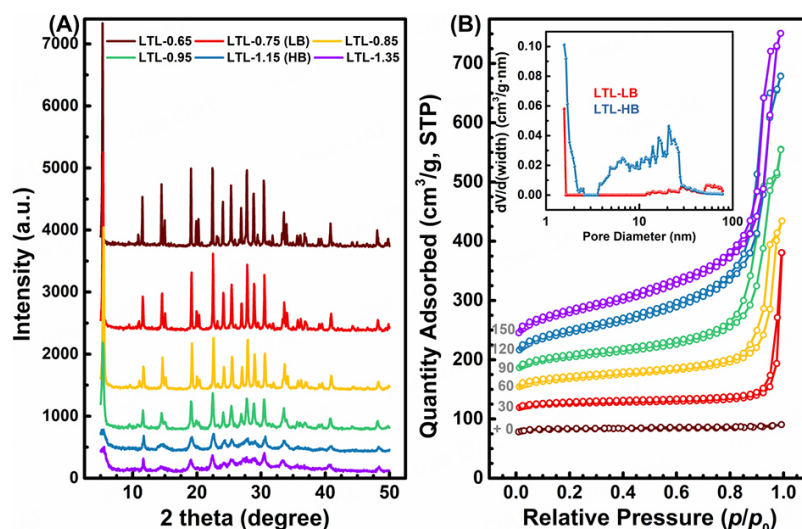
Figure 2. (A) XRD patterns and (B) N_2-sorption isotherms of different zeolite L samples. Inset of (B): mesopore size distribution of LTL-LB and LTL-HB.

the evolution of precursor structures and the distribution of nutrient species in the solid and liquid phases using two typical samples, LTL-LB (BSR = 0.75) and LTL-HB (BSR = 1.15). The intermediates at various crystallization intervals were collected and investigated (denoted as LTL-LB/HB-*t*, where *t* refers to the time of hydrothermal treatment; photographs with corresponding solid yields are displayed in Supplementary Figure 4). The solid-phase yield of the product is stable at approximately 32% in the LTL-LB system and 30% in the LTL-HB system.

The crystallization kinetic curves of LTL-LB and LTL-HB [Figure 3A and C] were obtained by the solid-phase XRD analysis [Supplementary Figure 5]. For LTL-LB-*t* [Figure 3A], the intermediates show no LTL characteristic peaks in the first 60 min of heating. Additionally, the relative crystallinity (RC) of the solid phase slowly increases to approximately 12% and then rapidly grows to 92% in the following 30 min (90 min of heating). For LTL-HB-*t* [Figure 3B], however, the higher alkalinity accelerates the crystallization process markedly, and RC increases by approximately 87% between *t* = 22 min and *t* = 44 min. Moreover, the compositions of the supernatant liquid were monitored together with the solid-phase SAR (i.e., changes in the Si-Al distribution). As shown in Supplementary Table 3, more than 2/3 of Al species in the clear precursor solution transfer into the solid phase when the gel network starts to form, and as RC increases, more Al species enter the solid phase synchronously. In contrast, changes in the concentration of Si species in the supernatant are not significantly different between the low and high BSR groups. The utilization rate of Al is more than 95% and that of Si is less than 30%; thus, further analysis of SAR changes in the solid and liquid phases provides a more intuitive picture of nutrient migration [Figure 3C and D]. As a result, a two-stage rise in the liquid-phase SAR and a corresponding piecewise fall in the solid-phase SAR can be clearly observed.

To determine the key nodes of the crystallization process and the cause of the plateau in the SAR curve, we analyzed the lower turning points of the above two curves. Serendipitously, we found that in this zeolite L system, the crystallization behaviors are strongly SAR-dependent. That is, the nucleation and subsequent growth of zeolites can occur only with an appropriate solid-phase SAR value, and thus the induction, nucleation, growth, and ripening stages of the crystallization process can be clearly distinguished [Figure 3]. After room temperature aging, both the low and high BSR systems become clear and transparent solutions.
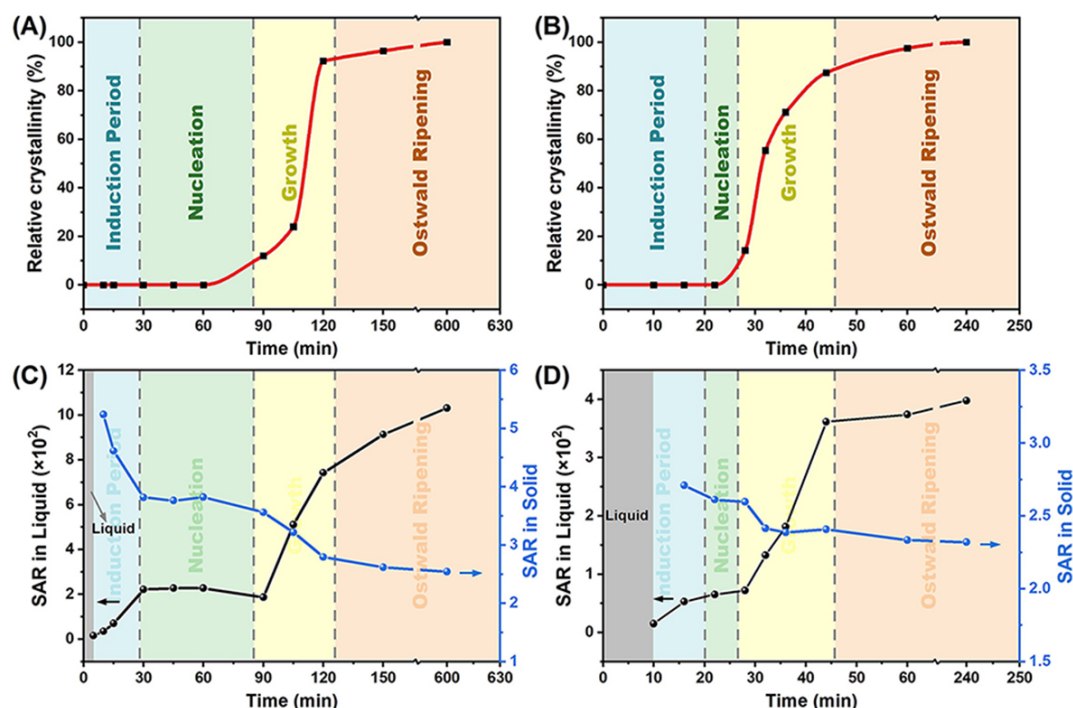
Figure 3. Kinetic curves of the crystal growth of (A) LTL-LB-*t* and (B) LTL-HB-*t*, according to the XRD data in Supplementary Figure 5. Related migration of Si and Al nutrients in the supernatant and solid phase of (C) LTL-LB-*t* and (D) LTL-HB-*t*, according to the data in Supplementary Table 3. The different colored regions represent four detailed stages of the crystallization process.

DLS measurements revealed that the clear liquid contains sol particles with a size of approximately 10 nm. For LTL-LB-*t* [Figure 3C], the solid gel phase is first observed when the clear initial sol is heated for 5 min. After that, the ICP-AES data shows a two-stage increase in SAR in the supernatant. Additionally, the data shows a relevant two-stage decline in SAR from 5.24 to 3.80 and then to 2.79 in the solid phase. Moreover, a rapid increase in crystallization can be observed from 60 to 120 min, which corresponds to the second changing period of SAR and indicates fast growth of **LTL**-type crystals. For LTL-HB-*t* [Figure 3D], a similar tendency of SAR in the liquid and solid occurs with a smaller change scale and in a shorter timeframe. Additionally, the increase in RC and the decrease in solid-phase SAR support the second SAR growth. Accordingly, the second SAR growth and solid-phase RC jump can be attributed to the "growth period" of zeolite crystallization (Figure 3, yellow regions).

It is generally accepted that **LTL** zeolites have a relatively low SAR and a limited regulation interval, similar to **FAU** and **LTA** zeolites with abundant 4-membered rings (4MRs)[52]. Because of this characteristic, **LTL** crystals can only form with a fixed SAR of 2-4 even for an initial mixture with a SAR above 10. Therefore, at the beginning of gel crosslinking, SAR in the solid phase is too high for the formation of LTL-type sub-units with short-range order (e.g., *d6r* and *can* containing 4MRs) in the amorphous matrix. The first decline of solid-phase SAR indicates an "induction period" in which the Si and Al nutrients exchange between the solid and liquid phases to reach the ratio for nucleation (Figure 3, blue regions). Subsequently, crystal nuclei form in concentrated areas with a suitable SAR, and SAR in the solid and liquid phases reaches a plateau (Figure 3, green region, "nucleation stage"). At the end of the "nucleation stage" and the beginning of the "growth stage", the characteristic Bragg peaks of **LTL** appear, and the peak intensity increases rapidly with increasing time. At this stage (Figure 3, yellow region), SAR of the solid phase shows a "secondary decline" until it is close to the final product, which suggests that for low-silica zeolites like **LTL**, further construction

of long-range order has more stringent elemental composition requirements than the formation of local nucleation domains. As RC increases to more than 80%, the change in SAR slows down again, indicating that the crystallization process reaches the final "Ostwald ripening stage" (Figure 3, orange region). At this stage, the crystal is formed to a large extent, and some small defects left by the rapid growth will be perfected through the slow liquid phase exchange process, which makes RC rise slowly and slightly. Moreover, as shown in Supplementary Figure 4, the solid-phase yield of time-resolved intermediates in the LTL-LB system shows a distinct two-stage descending feature. Specifically, the first stage is from 10 to 30 min, corresponding to the "Induction Period," and the second stage is from 90 to 120 min, corresponding to the "Growth Period." The two-stage descending feature indicates that there is significant element migration from the solid phase to the liquid phase during the induction and growth stages. However, the distinct two-stage descending feature does not emerge in the LTL-LB system, which can be attributed to the high alkalinity. The distribution of precursor species is fully optimized during the induction and growth periods due to the fast rate of material exchange, thus avoiding obvious fluctuations.

The start and end times of different stages in the whole crystallization process of LTL-LB and LTL-HB were successfully obtained. To further study the reasons for the formation of different morphologies, it is necessary to focus on two key stages - the nucleation stage and the growth stage - to figure out the detailed differences in the evolution behavior of intermediates under different BSR.

Investigation of the effects of BSR on Si-Al distribution/state
The Raman spectra of solid-phase intermediates were acquired to determine the effects of BSR on Si-Al distribution/state at the induction and nucleation stages [Figure 4A and D]. The band observed at 498 cm^{-1} with a shoulder at 470 cm^{-1} is attributed to the T-O-T bending mode of 4MRs in the LTL structure. Additionally, the increase in the band intensity represents the formation and evolution of short-range order[53]. For LTL-HB-*t*, compared with the XRD patterns [Supplementary Figure 5B] and RC curves [Figure 3B], the Raman spectra [Figure 4D] show that construction of the short-range structure starts early ($t = 16$ min, RC stays at 0% until $t = 22$ min) is approximately 80% complete within the next 16 min ($t = 32$ min, when RC = 55%). In contrast, for LTL-LB-*t*, progress starts at a late point ($t = 60$ min) and increases almost synchronously with the rise of RC (Figure 4A for Raman spectra, Figure 3A for RC curves).

The above results show that the length of the induction period is closely related to the formation of short-range order in the amorphous matrix. The different alkalinity conditions lead to distinct thermodynamic saturability of Si species, and thus the gel-network precipitated from the initial sol has dissimilar SAR values and different dynamic evolution phenomena. In the high alkalinity system (LTL-HB-*t*), the gel formed at 16 min with a SAR = 2.71 is suitable for the formation of **LTL**-type sub-units (e.g., 4MR-riched *can* cage), allowing rapid establishment of short-range order with a minor adjustment of nutrient distribution. For LTL-LB-*t*, however, the gel precipitated at 10 min contains too many Si species to form nuclei for zeolite L. Hence, a more significant and slower exchange of nutrients is detected between the solid and liquid phases as SAR in solid drops from ~5.2 to ~3.8 during the induction period. Consequently, a tediously long nucleation stage of more than 30 min is observed.

The chemical state of the Al atoms of the intermediates was investigated using solid-state ^{27}Al MAS NMR, as shown in Figure 4B and E. The signal of the tetrahedrally coordinated Al atoms of zeolite frameworks appears at a lower field than that of amorphous aluminosilicate, and the former is narrower than the latter due to improved homogeneity[39,54]. Therefore, the chemical shift and the corresponding full width at half maximum (FWHM) of the peaks of the intermediates obtained with different heating times are displayed in Figure 4C and F to evaluate the ordering process and the overall short-range uniformity, respectively. All
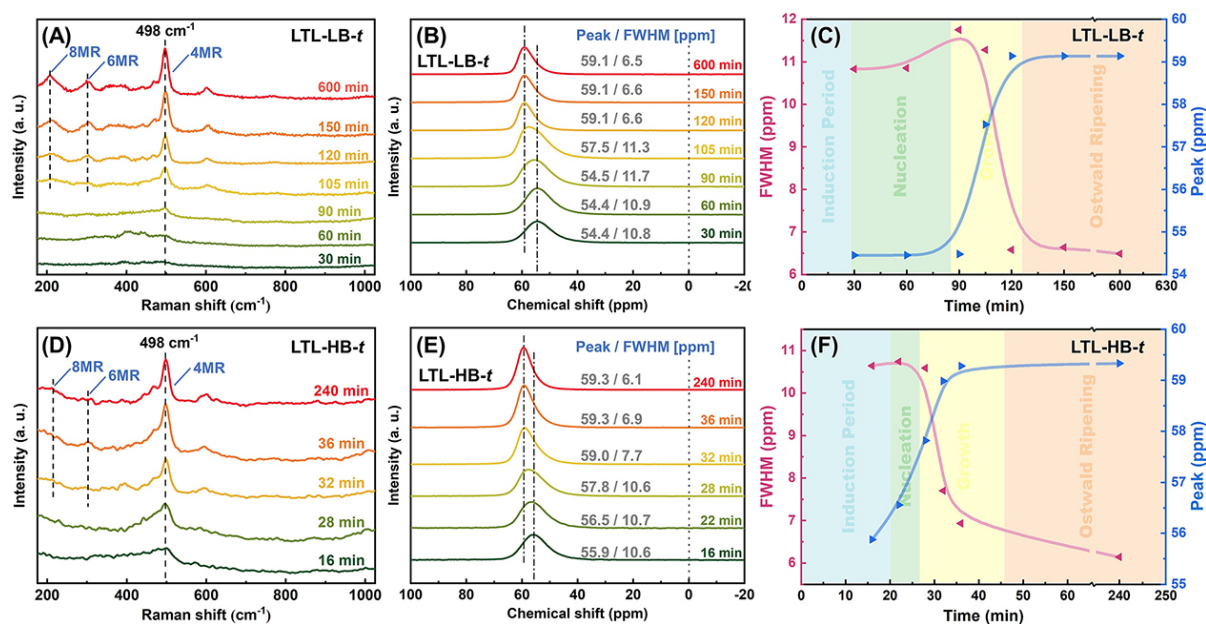
Figure 4. (A) Raman spectra, (B) ^{27}Al MAS NMR, and (C) related changes in the peak position and FWHM for LTL-LB-*t*. (D) Raman spectra, (E) ^{27}Al MAS NMR, and (F) related changes in the peak position and FWHM for LTL-HB-*t*.

samples show no peak at 0 ppm, indicating that all solid-phase Al atoms are tetrahedrally coordinated even in the amorphous precursors[39]. During the crystallization process, the ^{27}Al MAS NMR peaks of both systems shift to a lower field (from 54 to 59 ppm for LTL-LB-*t*, and 56 to 59 ppm for LTL-HB-*t*), which is consistent with reported results[54]. It is worth noting that in the LTL-LB system, signal shift begins at the start of the growth stage and continues until the end of this stage [Figure 4C]. In the LTL-HB system, the corresponding shift starts even before the middle of the nucleation stage and ends before the middle of the growth stage [Figure 4F]. Moreover, unlike the gradual decline in the FWHM of the LTL-HB-*t* peak [Figure 4F], the FWHM of the LTL-LB peak shows abnormal broadening in the nucleation stage and the early growth stage [Figure 4C]. The above results indicate that **LTL**-type sub-units can be established earlier and distributed widely in the gel network in the high alkalinity system, and the generation of more nucleation sites is conducive to rapid induced crystallization. In the low alkalinity system, however, relatively slower formation of less short-range ordered structures give birth to fewer nuclei and initial crystals, and other disordered species need to be assembled on the surface of these nuclei and initial crystals to become crystals gradually. Therefore, short-range order divergence under low and high alkalinity conditions directly leads to different crystallization kinetic behaviors.

Exploring the differentiated nucleation/growth behaviors of LTL-LB/HB-t
Different alkalinity conditions not only affect the nucleation speed/amount, they also change the detailed evolution mode of the precursors in the pre-nucleation stage. Visual evidence was obtained using TEM and dynamic light scatter (DLS) measurements. For LTL-LB, worm-like particles (WLPs) are formed by the crosslinking and collapsing processes of the gel networks, and the corresponding particle width increases from approximately 10 nm (*t* = 10 min) to 100-300 nm at *t* = 60 min [Supplementary Figures 6 and 7A]. This is accompanied with a few initial crystals of 5-20 nm in size [Figure 5A] at the gel-liquid boundary at 60 min. In the next 30 min, these small nuclei gradually grow to 50-100 nm in size, which is close to the width of WLPs [Figure 5B]. Moreover, the size of WLPs with a localized LTL crystalline phase gradually increases to 500 nm with larger aggregates (around 5 μm in size) at 90 min. During the growth and Ostwald ripening stages, from 90 to 600 min, the size of particles with increasing crystallinity remains at
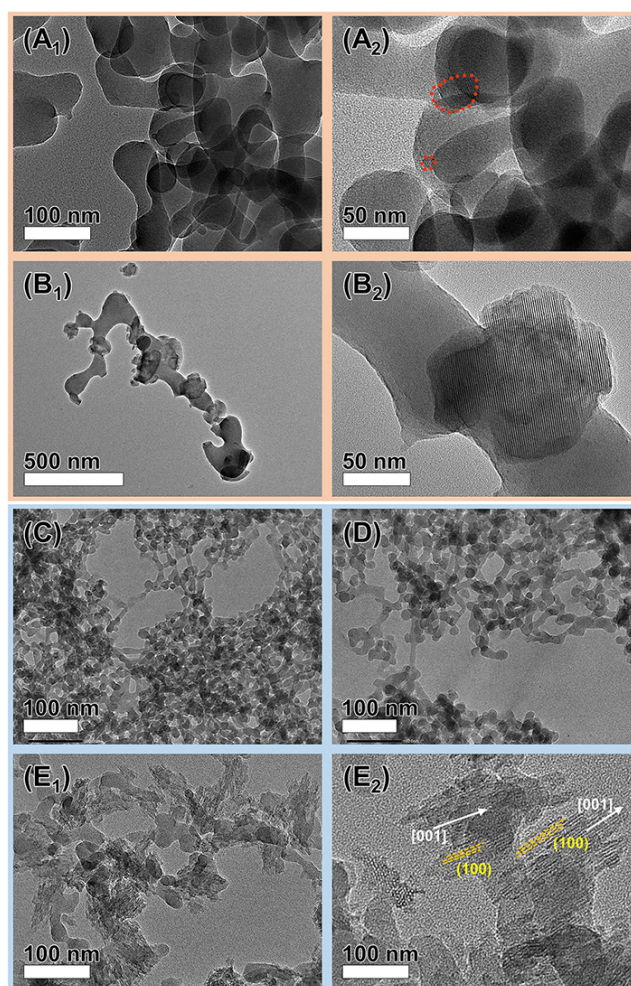
Figure 5. TEM images of LTL-LB-*t* in the nucleation stage and early growth stage: *t* = (A) 60 and (B) 90 min. TEM images of LTL-HB-*t* in the induction and nucleation stage: *t* = (C) 16, (D) 22, and (E) 28 min.

approximately 700 nm. In contrast, in the LTL-HB batch, WLPs formed at 16 min maintain the width of 15-20 nm throughout the induction period [Figure 5C and D, Supplementary Figure 7B] and give birth to abundant small crystals with a cluster-like morphology at 28 min (RC = 14%), of which the size is approximately 30 nm in width and approximately 50 nm in length [Figure 5E]. In the following stages, the particle size stays at 100-200 nm, which is significantly smaller than that of the LTL-LB system. A comparison of the above nucleation phenomena under different alkalinity conditions indicates that a relatively small number of nuclei (small crystals) are formed in the LTL-LB system. These initial crystals are generally located at the solid-liquid edges and show a single-crystal-like structure. In contrast, a large number of crystal nuclei can be formed in one WLP in the LTL-HB system, and it is notable that these adjacent nuclei mutually grow and adjust orientation, forming a prototype of nanocluster-like mesocrystals.

Prolonging the crystallization time to the growth stage leads to a rapid increase in RC, and the second change period of SAR can be observed. At this stage, the adjustment of solid-phase SAR in the high alkalinity system (from ~2.6 to ~2.4) [Figure 3D] is significantly smaller than that in the low alkalinity system (from ~3.6 to ~2.8) [Figure 3C], and the growth of corresponding relative Raman peak is also much faster, as mentioned above. It seems that the Si-Al nutrient distribution/state caused by different BSRs

further affects the growth stage. As our previous work revealed, differences in short-range order may lead to different assembly and/or induced growth modes between the amorphous and crystalline parts[37]. This conjecture was confirmed by TEM tracking. For LTL-LB-105, amorphous WLPs attach to the crystal surface and become crystalline through induced crystallization [Figure 6A]. A typical amorphous-to-crystalline conversion is displayed in Figure 6B. The composite structure with a crystalline core and an amorphous shell supports this "assembly, and induced crystallization" growth that occurs from inside the nuclei/crystal to outside the WLPs. In the following 15 min, WLPs in the LTL-LB system are consumed, and the corresponding RC value reaches approximately 92%. The morphology and size of the crystal are close to those of the final products [Figure 6C], suggesting the end of the rapid growth stage.

The induced crystallization process of LTL-HB in the growth stage is rather fast and somehow "*in-situ*". That is, in contrast to the "several WLPs"-to-"one crystal" assembly process in the low BSR system, one WLP may fracture to form several final crystals in the high BSR system. The TEM images show that abundant nucleation sites are generated in every single WLP (t = 28 min) [Figure 5E], and the subsequent induced crystallization process occurs rapidly along each WLP with multiple starts in the next 4 min, leading to the breakdown of WLPs and the formation of cluster-like products [Figure 7A]. This unique growth behavior also explains why the final products have a similar diameter and a significantly shorter length than WLP precursors. For LTL-HB-32, the RC value reaches approximately 55% without the appearance of an amorphous region, and the size/morphology of the crystals is similar to that of the final ones [Figure 1E]. This relatively low crystallinity suggests that there may be defects in the crystals. In the following growth and ripening stages, unused liquid Si and Al species grow on the crystals (inferred from the concentration change shown in Supplementary Table 3), which gives the zeolite smoother and sharper crystal edges and slightly increases the size of domains (Figure 7B for t = 60 min, Figure 1E for t = 240 min).

The formation of **LTL**-type microstructures is sensitive to the distribution/state of precursors Si and Al. Therefore, we further explored the distribution of the solid elements of two key intermediates. EDS results for LTL-LB-105 show an uneven distribution of Si and Al in the solid phase, and some Si-excess spheres can be observed (spot SAR = 4.3-7.2) [Supplementary Figure 8A]. Li *et al.* reported that zeolite synthesis systems commonly contain nonhomogeneous gel networks with Si-rich and Al-rich areas, especially when fumed silica or silica gel is used as the Si source[55]. Therefore, we postulated that the second drop in solid-phase SAR is due to nutrient exchange between the liquid phase and the Si-rich segments in WLPs to gain a suitable SAR for further crystal growth. As a result, parts of WLPs-located Si species undergo dynamic dissolution into the liquid phase during the induced crystallization process [Supplementary Table 3] or are extruded integrally (which eventually dissolves because no such particle is observed when the time is prolonged to more than 120 min). For LTL-HB-28 [Supplementary Figure 8B], conversely, EDS results show a fairly uniform distribution of Si and Al in the solid phase, and the detailed SAR value matches the final framework SAR. This uniformity and compatibility ensure the rapid and extensive formation of **LTL** microstructure at the thermodynamic level.

The texture of intermediates was characterized using N_2-sorption experiments [Supplementary Figure 9 and Supplementary Table 4]. Generally, the zeolitic micropore surface and volume (S_{micro} and V_{micro}) grow with a relative lag as the RC value increases. To quantify the magnitude of the hysteresis, the relative V_{micro} (RV, which is defined as the ratio of "V_{micro} of the intermediate" to "V_{micro} of the final product") of intermediates was calculated and compared with the corresponding RC values [Supplementary Table 4]. It can be seen that this delayed formation of zeolitic micropores is more obvious in the low BSR system (LTL-LB-t) because the RV/RC ratio remains low (< 0.3) throughout the early growth stage ($t \leq 105$ min). That is, at this stage, the generated small crystals/nuclei in the LTL-LB-t system have a relatively complete **LTL**-type
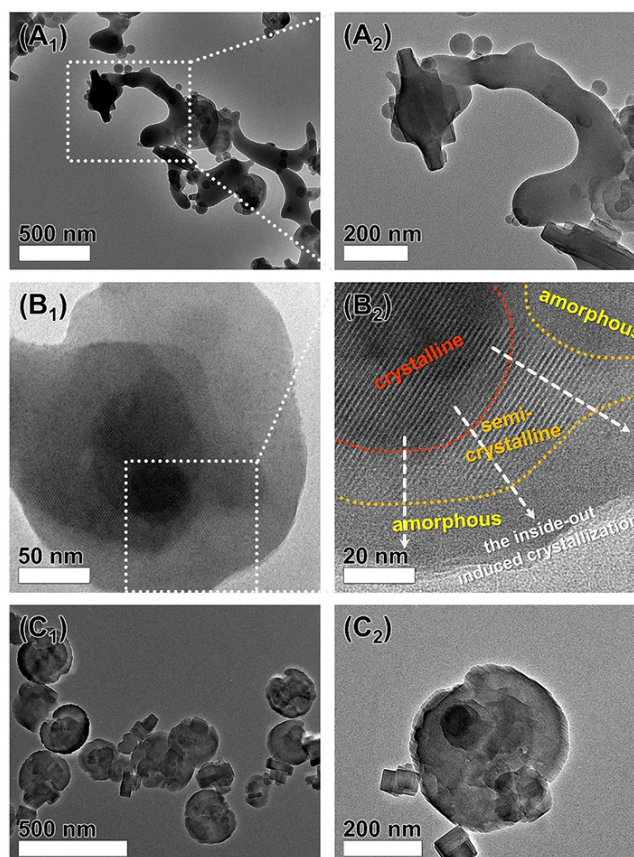
Figure 6. TEM images of (A) the assembly behavior between WLPs and crystals for LTL-LB-105. (B) Inside-out induced crystallization process for LTL-LB-105. (C) Crystals in LTL-LB-120.

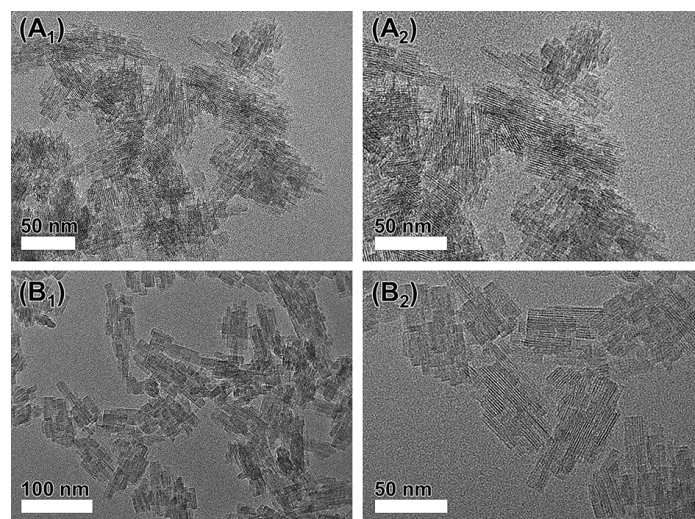**Figure 7.** TEM images of LTL-HB in the growth and ripening stages: t = (A) 32 and (B) 60 min.

crystalline structure, while there are almost no initial zeolitic pores in the amorphous parts. When these disordered WLPs start to wrap around the outside of the crystalline part, the outermost amorphous layer hinders connectivity to the inner crystal micropores, making the measured RV relatively low. Subsequently,

corresponding with the rapid rise in RC, a sharp increase in V_{micro} from 0.009 to 0.140 cm^3/g can be seen between 105-120 min, which is attributed to the inside-out induced crystallization of WLPs and the re-opening of microporous channels. In contrast, subsequent ripening only results in a reduction in the mesoporous volume and surface (V_{meso} and S_{ext}). For the high BSR group (LTL-HB-*t*), in contrast, the lag of RV is smaller than that of RC. After the lattice fringes are first observed in the TEM images (*t* = 28 min, RC = 14%), the RV/RC ratio remains high (> 0.55) [Supplementary Table 4]. This indicates that the amorphous WLPs in the LTL-HB system have a good microstructure. With the rapid occurrence of *in situ* induced crystallization, **LTL**-type micropores can be constructed and penetrated rapidly. This behavior is consistent with the short-range ordering information obtained through Raman and NMR experiments.

Putative crystallization mechanism and its validation

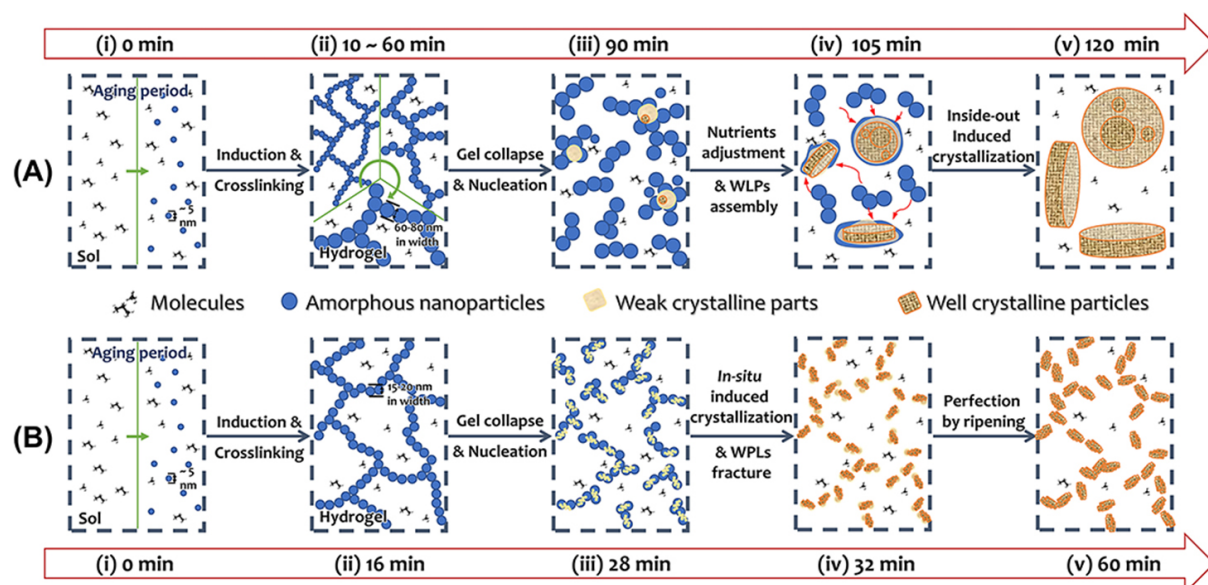*Uncovering the nonclassical crystallization mechanism of LTL-LB/HB-t*
By comparing the evolution behaviors under different alkalinity conditions, it is evident that BSR influences the solubility of Si species, which in turn affects the thermodynamic properties of amorphous precursors, such as the non/uniformity of Si and Al distributions and the high/low potential to form **LTL**-type microstructures, leading to different crystallization kinetics and products with various morphologies. In the aging stage, the reaction mixture in both systems is a clear solution owing to the relatively high pH [Scheme 1A(i) and Scheme 1B(i)]. As the temperature rises, colloidal silica particles aggregate, the gel network begins to form [Scheme 1A(ii) and Scheme 1B(ii)], and tetra-coordinated Al enters the solid-phase gel network. At this gel formation stage, BSR affects the solubility of Si species and the stability of the ≡Si-O-Si≡ bond. Under low alkalinity conditions (LTL-LB), the gel network has a higher degree of crosslinking, with more Si species entering the solid phase and producing a coarser gel network [Scheme 1A(ii)]. Moreover, owing to the low solubility of Si and the relatively slow exchange rate between the solid and liquid phases, the distribution of Si and Al in the solid phase is not uniform, and some localized Si-rich zones exist [Supplementary Figure 8A]. Conversely, as the alkalinity increases (LTL-HB), the solubility of Si species increases, and mass exchange is also faster, resulting in a narrower-sized gel network with a relatively homogeneous distribution of elements [Scheme 1B(ii) and Supplementary Figure 8B].

After the rearrangement of elements in the gel network and the formation of WLPs by fracture of the gel network, regions of solid-phase particles with more suitable SAR show a preference for nucleation late in the induction period. Since the SAR of LTL-HB precursors closely matches the **LTL** structure, a large number of nucleation sites rapidly form in adjacent regions, which are subsequently adjusted to produce oriented cluster-like nuclei [Scheme 1B(iii)]. For LTL-LB, however, the unsuitable initial SAR of the solid phase and the relatively slow mass transfer lead to a significantly longer induction period, and the nucleation sites are fewer and located mainly at the solid-liquid junction, where mass exchange, element adjustment, and the formation of 4MR sub-units occur easily [Scheme 1A(iii)].

In the subsequent growth stage, amorphous WLPs in the LTL-LB system aggregate on the nuclei surface [Scheme 1A(iv)]. Owing to the unsuitable SAR and the lack of short-range ordered microstructure, the inside-out induced crystallization process [Scheme 1A(v)] is assisted by solid-liquid element transfer, leading to a significant change in SAR in the gel and solution phases [Figure 3C]. In contrast, in the LTL-HB system, the amorphous part shows good short-range order. As a result, direct and rapid induced crystallization occurs *in situ* [Scheme 1B(iv) and (v)], along with a relatively less involved liquid-phase process (because changes in the elements in solution are smaller) [Figure 3D].

Mechanism validation by analyzing morphology evolution, NH₄F etching, and the effects of modifiers and K⁺
The above assumptions are supported by the changes in crystal morphology under different alkalinity

Scheme 1. Putative nonclassical crystallization pathways of (A) LTL-LB and (B) LTL-HB.

conditions. In the cylindrical/disc-like morphology region (Figure 1A-C, BSR ≤ 0.85), low alkalinity amplifies the unsuitable initial SAR and slow adjustment of elements in the solid phase, which drastically decreases the crystallization rate [Supplementary Table 1]. Moreover, the nonuniform Si-Al distribution and poor short-range order in amorphous precursors greatly inhibit nucleation. That is, the number of WLPs assembled on each nucleus increases, leading to a significant enlargement of the final products. Additionally, owing to the slower attachment and internal reorganization of WLPs, the classical mechanism (growth via the addition of simple species) of crystallization is prominent, resulting in a dense product and a rise in the c/a-axis ratio. A previous study found that in the growth of disc-shaped zeolite L, the attachment of simple molecules preferentially occurs along the c-axis[44]. In the nanocrystal/nanocluster region (Figure 1D-F, BSR ≥ 0.85), however, high alkalinity boosts nucleation, resulting in a decrease in the size of each domain. Moreover, the proximity of nucleation sites to one WLP facilitates interlacing, leading to the formation of large oriented clusters.

To further verify this crystallization mechanism, NH_4F etching experiments and synthesis in the presence of modifiers were carried out for LTL-LB and LTL-HB. NH_4F tends to etch high-energy interfaces in zeolite, thus revealing hidden building blocks[28]. After NH_4F etching of LTL-LB, the remaining parts show a cashew-like shape with a width of 50-80 nm, which is similar to WLPs [Figure 8A], confirming that crystals are formed by the assembly and fusion of WLPs. In contrast, after NH_4F etching of LTL-HB, the particles retain their overall shape, while the nanoclusters become looser and the pores between adjacent domains are larger [Figure 8B], which is consistent with the assumption that neighboring nuclei form interlaced nanoclusters in a single WLP.

During the assembly of WLPs to form micron-sized zeolite L, the product aspect ratio can be altered by using modifiers n-BuNH$_2$ and PDDAC to suppress WLPs-crystal deposition along the c-axis and a/b-axis, respectively[35]. Experiments were conducted in which modifiers n-BuNH$_2$ and PDDAC were introduced into the LTL-LB and LTL-HB systems. The results show that the morphology of LTL-LB is sensitive to both n-BuNH$_2$ [Figure 8C] and PDDAC [Figure 8E], while that of LTL-HB is unaffected by the modifiers [Figure 8D and F]. These results further confirm that one cylindrical/disc-shaped zeolite crystal may
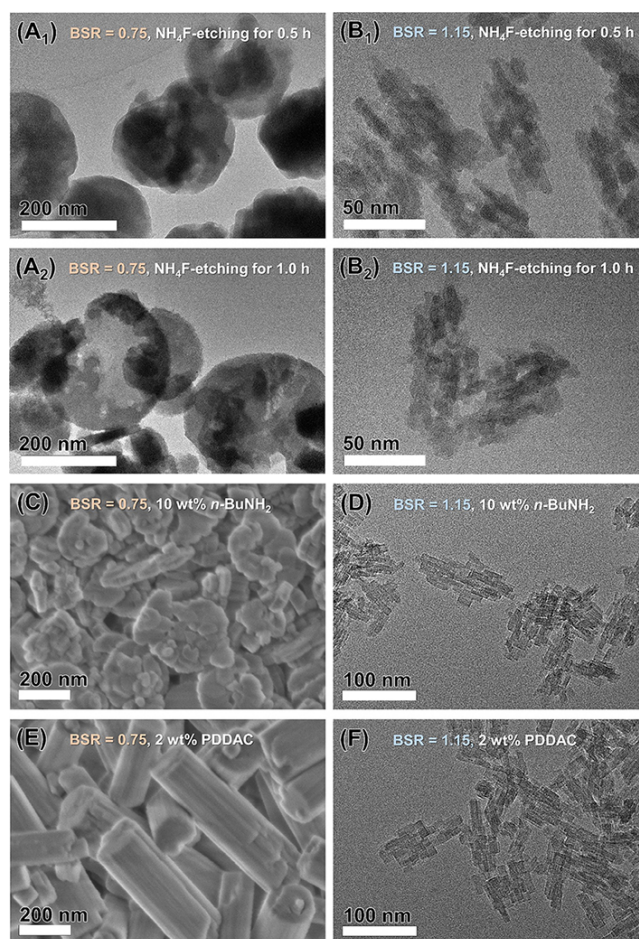
Figure 8. TEM images of (A) NH$_4$F-etched LTL-LB and (B) NH$_4$F-etched LTL-HB. Products obtained under (C and E) BSR = 0.75 and (D and F) BSR = 1.15 with the addition of modifiers *n*-BuNH$_2$ (C and D) and PDDAC (E and F).

originate from the aggregation of multiple WLPs, while the formation of one nanocluster zeolite L does not involve the assembly of WLPs but originates from a single WLP with *in situ* interleaved nucleation and induced crystallization.

In addition, the presence of KOH affects the concentration of K$^+$ in the system, although the above discussion is mainly focused on the thermodynamic and kinetic effects of system alkalinity (OH$^-$ concentration) on the crystallization mechanism. Therefore, it is also necessary to consider whether changes in the K$^+$ concentration affect the product morphology. In the original LTL-HB system (BSR = 1.15), an equimolar amount of NaOH was used to replace a proportion of KOH. This operation has a slight effect on the product morphology; specifically, the products remain nanoclusters, although the overall particle size and domain size increase slightly with the decrease in K$^+$/SiO$_2$ from 1.15 to 0.75 and 0.55 [Supplementary Figure 10]. Moreover, EDS results show that the Na$^+$/K$^+$ molar ratios in the two products with the feeding NaOH/KOH ratios of 0.4:0.75 and 0.6:0.55 are respectively 0.033 and 0.060, indicating that the counterion is mainly K$^+$. It should be noted that if a greater proportion of K$^+$ is replaced with Na$^+$ (K$^+$/SiO$_2$ < 0.5, when OH$^-$/SiO$_2$ = 1.15), then pure **LTL** phase zeolite is unavailable because it is generally believed that K$^+$ can just hold the **can** cage and acts as a special structure-directing agent for **LTL**[56]. These experiments indicate that as long as sufficient K$^+$ participates in the formation of microstructures, it is the alkalinity (OH$^-$) that plays a dominant role in the regulation of crystallization and morphologies of zeolite L. Further increasing or

decreasing excessive K^+ has no obvious effect on morphology control.

Adsorption performances of zeolite L mesocrystals with different morphologies

Changing BSR in the synthesis system also changes the morphology, including texture, size, exposed crystal face, and micropore length, of the obtained zeolite L, which affects the properties of the zeolite. Morphological and architectural changes in zeolite L can be reflected in the adsorption of probe molecules with various sizes and properties, thus further guiding the preparation of purpose-directed zeolite adsorbents and functional materials. Therefore, the adsorption of gaseous aromatic hydrocarbons, dye solutions, and proteins was investigated as three typical applications with environmental or biological value.

For the gas-phase adsorption of aromatic hydrocarbons, LTL-HB with a larger S_{ext} exhibits a higher adsorption capacity for both *o*-xylene (kinetic diameter = 0.65nm) and 1,3,5-triethyl benzene (kinetic diameter = 0.82 nm) than LTL-LB [Supplementary Figure 11A]. The rapid adsorption of *o*-xylene (which can enter the micropore channels of zeolite L) by the nanocluster-shaped L zeolite is an obvious advantage (Figure 9A and Supplementary Figure 11B, inset). The characteristic diffusion time (L_0^2/D, see the discussion for Supplementary Figure 11 in the supporting information) was calculated. LTL-HB (L_0^2/D = 0.888 s) has a significantly shorter characteristic diffusion time than LTL-LB (L_0^2/D = 76.9 s) [Figure 9A], which correlates with the length of the micropore channels along the [001] direction, specifically the former is approximately 1/7 the length of the latter. The above results indicate that nanocluster-shaped zeolite L is more suitable than cylindrical/disc-shaped zeolite L for the adsorption of gas phase aromatic hydrocarbons because the former has a shorter *c*-axis length and larger specific surface area than the latter.

For the liquid-phase adsorption of methylene blue (molecular dimensions: 1.43 nm × 0.61 nm × 0.40 nm), similar dynamic phenomena were observed [Figure 9B]. Specifically, adsorption by clustered zeolite L (LTL-HB) is significantly faster than adsorption by disc-shaped zeolite (LTL-LB). For LTL-HB, the adsorption efficiency reaches 73.6% in 20 s and 100% in 20 min. For LTL-LB, the efficiency is only 41.5% in the first 20 s and below 90% in 60 min [Figure 9B]. The effect of the initial probe concentration on the equilibrium adsorption capacity of LTL-HB and LTL-LB was also evaluated [Supplementary Figure 12A-C]. The adsorption curve of methylene blue on LTL-LB has typical characteristics of the Langmuir model, while that of methylene blue on LTL-HB has mixed features of the Langmuir and multi-layer adsorption models[57,58]. This thermodynamic adsorption feature indicates that the dye molecules are simultaneously adsorbed on the microporous channels and the external surface of the zeolite. Additionally, the dye adsorption capacities of all six zeolite L samples were evaluated. The results show that the LTL-1.35 sample with the largest S_{ext} and smallest domain size exhibits the highest adsorption capacity [Supplementary Figure 12D].

Nanocrystal zeolite L obtained with BSR = 0.95 displays the highest adsorption capacity for myoglobin (molecular dimensions: 4.5 nm × 3.5 nm × 2.5 nm), while nanoclusters with higher S_{ext} have lower adsorption capacities for myoglobin [Supplementary Figure 13A]. Because proteins such as myoglobin are large, they can only be adsorbed on the outermost surface of the crystal, and the gaps between adjacent domains in the nanoclusters become inaccessible. Additionally, our previous work showed that the protein adsorption capacity of the (001) face of zeolite L is approximately 10 times that of the (100)/(010) face[59]. An analysis of the adsorption data using the definition of the effective adsorption specific area ($A_{eff} = 5/L+1/R$, see the discussion for Supplementary Figure 13) revealed a good linear relationship between the amount of adsorbed myoglobin and the A_{eff} of zeolite L with different morphologies [Figure 9C]. This finding facilitates future designs of zeotype supports with suitable morphologies for protein and enzyme immobilization.
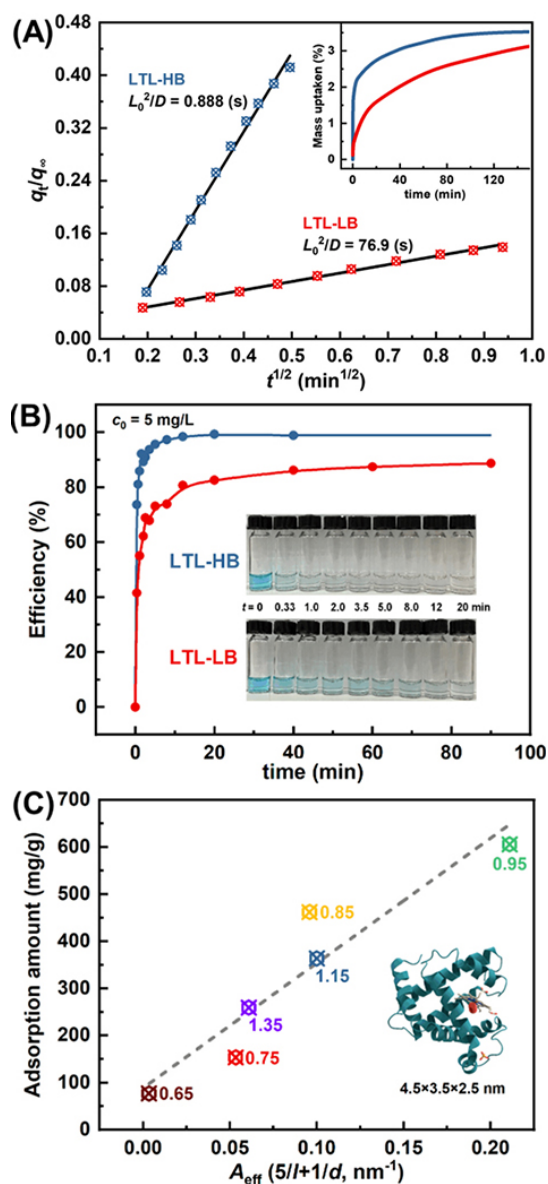
Figure 9. (A) Characteristic diffusion times of *o*-xylene on different zeolite L calculated using the kinetic uptake profiles (inset) in the short time domain (p/p_0 = 0→0.05). (B) Adsorption kinetic curves of methylene blue on LTL-LB/HB. Inset: corresponding photographs. (C) Relationship between the defined factor A_{eff} of different zeolite L with the corresponding adsorption capacity of myoglobin. Inset: molecular structure and size of myoglobin.

CONCLUSIONS

By simply adjusting the alkalinity of the synthesis system, a series of **LTL** mesocrystals with almost all morphologies (from cylindrical/disc-like shapes to nanoclusters/nanocrystals) were synthesized rapidly (1-2 h). The obtained zeolite products with different molecular dimensions and states exhibited excellent adsorption performance. Comprehensive tracking of the evolution of long-range/short-range order and the distribution of solid/ liquid nutrients throughout the crystallization process revealed that the above morphological shift is achieved by a two-step thermodynamic/kinetic co-regulation mechanism: First, different basicity conditions lead to thermodynamic differences in the precursors, such as non/uniformity of elemental distribution and high/low potential for microstructure formation. Subsequently, these

thermodynamic differences in the precursors induce different crystallization kinetic behaviors. That is, the assembly of WLPs on discrete single crystal-like nuclei in the low BSR system, and *in situ* induced crystallization along a single WLP in the high BSR system. Notably, an analysis of crystal growth and nutrient migration in these systems provided a standardized model for zeolite formation comprising four stages of crystallization, namely induction, nucleation, growth, and ripening. A related nonclassical crystallization mechanism was uncovered for zeolite L when different alkalinity conditions were employed, and its validity was evaluated by analyzing morphology evolution, NH_4F etching of the obtained mesocrystals, and effects of modifiers and K^+. The results presented herein not only provide insight into an understanding of the evolution of crystalline materials but also pave a new way for the economical and green synthesis of target-oriented zeotype materials.

DECLARATIONS

Authors' contributions

Conceptualization, investigation, data curation, formal analysis, writing - original draft, visualization: Ye Z

Formal analysis, validation, data curation, writing - review & editing: Kong L

Formal analysis, validation, data curation: Zhao Y

Investigation, methodology, validation: Zhang C, Yang X, Yan K

Resources, formal analysis, writing - review & editing: Zhang Y

Resources, conceptualization, formal analysis, visualization, writing - review & editing: Zhang H

Resources, formal analysis, writing - review & editing, supervision, project administration: Tang Y

Availability of data and materials

The authors confirm that the data supporting the findings of this study are available within its Supplementary Materials.

Conflicts of interest

The authors declared that they have no known competing financial interests or personal relationships that could have appeared to influence the work reported in this paper.

Ethical approval and consent to participate

Not applicable.

Consent for publication

Not applicable.

REFERENCES

1. Rimer JD, Chawla A, Le TT. Crystal engineering for catalysis. *Annu Rev Chem Biomol Eng* 2018;9:283-309. DOI PubMed
2. Dandekar P, Kuvadia ZB, Doherty MF. Engineering crystal morphology. *Annu Rev Mater Res* 2013;43:359-86. DOI
3. Lai WH, Wang YX, Wang Y, et al. Morphology tuning of inorganic nanomaterials grown by precipitation through control of electrolytic dissociation and supersaturation. *Nat Chem* 2019;11:695-701. DOI PubMed
4. Görke M, Garnweitner G. Crystal engineering of nanomaterials: current insights and prospects. *CrystEngComm* 2021;23:7916-27. DOI

5.   Brammer L. Developments in inorganic crystal engineering. *Chem Soc Rev* 2004;33:476-89. DOI PubMed

6.   Zhou W. Reversed crystal growth: implications for crystal engineering. *Adv Mater* 2010;22:3086-92. DOI PubMed

7.   Desiraju GR. Crystal engineering: a holistic view. *Angew Chem Int Ed Engl* 2007;46:8342-56. DOI PubMed

8.   Jain R, Mallette AJ, Rimer JD. Controlling nucleation pathways in zeolite crystallization: seeding conceptual methodologies for advanced materials design. *J Am Chem Soc* 2021;143:21446-60. DOI PubMed

9.   Olafson KN, Li R, Alamani BG, Rimer JD. Engineering crystal modifiers: bridging classical and nonclassical crystallization. *Chem Mater* 2016;28:8453-65. DOI

10.   De Yoreo JJ, Gilbert PU, Sommerdijk NA, et al. Crystal growth. Crystallization by particle attachment in synthetic, biogenic, and geologic environments. *Science* 2015;349:aaa6760. DOI PubMed

11.   Kirschhock CEA, Ravishankar R, Jacobs PA, Martens JA. Aggregation mechanism of nanoslabs with zeolite MFI-type structure. *J Phys Chem B* 1999;103:11021-7. DOI

12.   Sheng Z, Li H, Du K, et al. Observing a zeolite nucleus (subcrystal) with a uniform framework structure and its oriented attachment without single-molecule addition. *Angew Chem Int Ed Engl* 2021;60:13444-51. DOI PubMed

13.   Davis TM, Drews TO, Ramanan H, et al. Mechanistic principles of nanoparticle evolution to zeolite crystals. *Nat Mater* 2006;5:400-8. DOI PubMed

14.   He G, Dahl T, Veis A, George A. Nucleation of apatite crystals in vitro by self-assembled dentin matrix protein 1. *Nat Mater* 2003;2:552-8. DOI PubMed

15.   Fang Y, Hu H, Chen G. In situ assembly of zeolite nanocrystals into mesoporous aggregate with single-crystal-like morphology without secondary template. *Chem Mater* 2008;20:1670-2. DOI

16.   Zhang H, Ma Y, Song K, Zhang Y, Tang Y. Nano-crystallite oriented self-assembled ZSM-5 zeolite and its LDPE cracking properties: Effects of accessibility and strength of acid sites. *J Catal* 2013;302:115-25. DOI

17.   Niederberger M, Cölfen H. Oriented attachment and mesocrystals: non-classical crystallization mechanisms based on nanoparticle assembly. *Phys Chem Chem Phys* 2006;8:3271-87. DOI PubMed

18.   Song RQ, Cölfen H. Mesocrystals-ordered nanoparticle superstructures. *Adv Mater* 2010;22:1301-30. DOI PubMed

19.   Sturm Née Rosseeva EV, Cölfen H. Mesocrystals: structural and morphogenetic aspects. *Chem Soc Rev* 2016;45:5821-33. DOI PubMed

20.   Shamzhy M, Opanasenko M, Concepción P, Martínez A. New trends in tailoring active sites in zeolite-based catalysts. *Chem Soc Rev* 2019;48:1095-149. DOI PubMed

21.   Choi M, Na K, Kim J, Sakamoto Y, Terasaki O, Ryoo R. Stable single-unit-cell nanosheets of zeolite MFI as active and long-lived catalysts. *Nature* 2009;461:246-9. DOI PubMed

22.   Zhang Y, Che S. π-π interactions between aromatic groups in amphiphilic molecules: directing hierarchical growth of porous zeolites. *Angew Chem Int Ed Engl* 2020;59:50-60. DOI PubMed

23.   Korde A, Min B, Kapaca E, et al. Single-walled zeolitic nanotubes. *Science* 2022;375:62-6. DOI PubMed

24.   Jacobsen CJH, Madsen C, Houzvicka J, Schmidt I, Carlsson A. Mesoporous zeolite single crystals. *J Am Chem Soc* 2000;122:7116-7. DOI

25.   Azhati A, Xie S, Wang W, et al. Ordered, highly zeolitized mesoporous aluminosilicates produced by a gradient acidic assembly growth strategy in a mixed template system. *Chem Mater* 2016;28:4859-66. DOI

26.   Sun MH, Chen LH, Yu S, et al. Micron-sized zeolite beta single crystals featuring intracrystal interconnected ordered macro-meso-microporosity displaying superior catalytic performance. *Angew Chem Int Ed Engl* 2020;59:19582-91. DOI PubMed

27.   Jung J, Jo C, Mota FM, Cho J, Ryoo R. Acid catalytic function of mesopore walls generated by MFI zeolite desilication in comparison with external surfaces of MFI zeolite nanosheet. *Appl Catal A-Gen* 2015;492:68-75. DOI

28.   Qin Z, Melinte G, Gilson JP, et al. The mosaic structure of zeolite crystals. *Angew Chem Int Ed Engl* 2016;55:15049-52. DOI PubMed

29.   Zhang B, Zhang Y, Hu Y, et al. Microexplosion under microwave irradiation: a facile approach to create mesopores in zeolites. *Chem Mater* 2016;28:2757-67. DOI

30.   Ren N, Subotić B, Bronić J, et al. Unusual pathway of crystallization of zeolite ZSM-5 in a heterogeneous system: phenomenology and starting considerations. *Chem Mater* 2012;24:1726-37. DOI

31.   Zhang Q, Mayoral A, Terasaki O, et al. Amino acid-assisted construction of single-crystalline hierarchical nanozeolites via oriented-aggregation and intraparticle ripening. *J Am Chem Soc* 2019;141:3772-6. DOI PubMed

32.   Zhang Q, Chen G, Wang Y, et al. High-quality single-crystalline MFI-type nanozeolites: a facile synthetic strategy and MTP catalytic studies. *Chem Mater* 2018;30:2750-8. DOI

33.   Zhang H, Zhao Y, Zhang H, et al. Tailoring zeolite ZSM-5 crystal morphology/porosity through flexible utilization of silicalite-1 seeds as templates: unusual crystallization pathways in a heterogeneous system. *Chem Eur J* 2016;22:7141-51. DOI PubMed

34.   Kumar M, Luo H, Román-Leshkov Y, Rimer JD. SSZ-13 crystallization by particle attachment and deterministic pathways to crystal size control. *J Am Chem Soc* 2015;137:13007-17. DOI PubMed

35.   Lupulescu AI, Kumar M, Rimer JD. A facile strategy to design zeolite L crystals with tunable morphology and surface architecture. *J Am Chem Soc* 2013;135:6608-17. DOI PubMed

36.   Zheng J, Zhang W, Liu Z, et al. Unraveling the non-classic crystallization of SAPO-34 in a dry gel system towards controlling meso-structure with the assistance of growth inhibitor: growth mechanism, hierarchical structure control and catalytic properties.

Microporous Mesoporous Mater 2016;225:74-87. DOI

37. Ye Z, Zhao Y, Zhang H, et al. Mesocrystal morphology regulation by "alkali metals ion switch": re-examining zeolite nonclassical crystallization in seed-induced process. *J Colloid Interface Sci* 2022;608:1366-76. DOI PubMed

38. Zhang H, Zhang H, Zhao Y, Shi Z, Zhang Y, Tang Y. Seeding bundlelike MFI zeolite mesocrystals: a dynamic, nonclassical crystallization via epitaxially anisotropic growth. *Chem Mater* 2017;29:9247-55. DOI

39. Zhao Y, Zhang H, Wang P, et al. Tailoring the morphology of MTW zeolite mesocrystals: intertwined classical/nonclassical crystallization. *Chem Mater* 2017;29:3387-96. DOI

40. Wang L, Zhu SC, Shen MK, et al. Fractal MTW zeolite crystals: hidden dimensions in nanoporous materials. *Angew Chem Int Ed Engl* 2017;56:11764-8. DOI PubMed

41. Wang P, Zhao Y, Zhang H, Yu T, Zhang Y, Tang Y. Effect of pyrazolium-derived compounds as templates in zeolite synthesis. *RSC Adv* 2017;7:23272-8. DOI

42. Ruiz AZ, Brühwiler D, Ban T, Calzaferri G. Synthesis of zeolite L. Tuning size and morphology. *Monatsh Chem* 2005;136:77-89. DOI

43. Hu Y, Liu C, Zhang Y, Ren N, Tang Y. Microwave-assisted hydrothermal synthesis of nanozeolites with controllable size. *Microporous Mesoporous Mater* 2009;119:306-14. DOI

44. Larlus O, Valtchev VP. Crystal morphology control of LTL-type zeolite crystals. *Chem Mater* 2004;16:3381-9. DOI

45. Meier WM, Olson DH, Baerlocher C. Atlas of zeolite structure types. *Zeolites* 1996. Available from: https://www.researchgate.net/publication/248827852_Atlas_of_Zeolite_Structure_Types [Last accessed on 25 Nov 2022]

46. Itani L, Bozhilov KN, Clet G, Delmotte L, Valtchev V. Factors that control zeolite L crystal size. *Chem Eur J* 2011;17:2199-210. DOI PubMed

47. Kumar M, Li R, Rimer JD. Assembly and evolution of amorphous precursors in zeolite L crystallization. *Chem Mater* 2016;28:1714-27. DOI

48. Thommes M, Kaneko K, Neimark AV, et al. Physisorption of gases, with special reference to the evaluation of surface area and pore size distribution (IUPAC Technical Report). *Pure Appl Chem* 2015;87:1051-69. DOI

49. Devi R, Borah R, Deka RC. Design of zeolite catalysts for nitroaldol reaction under mild condition. *Appl Catal A-Gen* 2012;433-434:122-7. DOI

50. Tangale NP, Sonar SK, Niphadkar PS, Joshi PN. Hierarchical K/LTL zeolites: synthesis by alkali treatment, characterization and catalytic performance in Knoevenagel condensation reaction. *J Ind Eng Chem* 2016;40:128-36. DOI

51. Joshi PN, Jacob NE, Shiralkar VP. Physicochemical characterization of the intermediate phases obtained during the hydrothermal crystallization of LTL zeolites. *J Phys Chem* 1995;99:4225-9. DOI

52. Oleksiak MD, Soltis JA, Conato MT, Penn RL, Rimer JD. Nucleation of FAU and LTA zeolites from heterogeneous aluminosilicate precursors. *Chem Mater* 2016;28:4906-16. DOI

53. Dutta PK, Shieh DC. Crystallization of zeolite A: a spectroscopic study. *J Phys Chem* 1986;90:2331-4. DOI

54. Chen CT, Iyoki K, Hu P, et al. Reaction kinetics regulated formation of short-range order in an amorphous matrix during zeolite crystallization. *J Am Chem Soc* 2021;143:10986-97. DOI PubMed

55. Li R, Linares N, Sutjianto JG, Chawla A, Garcia-Martinez J, Rimer JD. Ultrasmall zeolite L crystals prepared from highly interdispersed alkali-silicate precursors. *Angew Chem Int Ed Engl* 2018;57:11283-8. DOI PubMed

56. Ohgushi T, Matsuo T, Satoh H, Matsumoto T. Cation distribution in K,H-L zeolite prepared through ion-exchange with TMA ion. *Microporous Mesoporous Mater* 2009;117:472-7. DOI

57. Bulut E, Özacar M, Şengil İA. Adsorption of malachite green onto bentonite: Equilibrium and kinetic studies and process design. *Microporous Mesoporous Mater* 2008;115:234-46. DOI

58. Choy KKH, Porter JF, Mckay G. Langmuir isotherm models applied to the multicomponent sorption of acid dyes from effluent onto activated carbon. *J Chem Eng Data* 2000;45:575-84. DOI

59. Hu Y, Zhang Y, Ren N, Tang Y. Crystal plane- and size-dependent protein adsorption on nanozeolite. *J Phys Chem C* 2009;113:18040-6. DOI